JOURNAL OF AIRCRAFT
Vol. 45, No. 2, March–April 2008

Aerodynamic Characteristics of Elliptic Airfoils at High Reynolds Numbers

Sungyoon Choi* and Oh Joon Kwon†
Korea Advanced Institute of Science and Technology, Daejeon 305-701, Republic of Korea

DOI: 10.2514/1.32671

In the present study, the aerodynamic characteristics of elliptic airfoils were numerically investigated based on the Reynolds-averaged Navier–Stokes equations and the Spalart–Allmaras one-equation turbulence model. Calculations were performed for several Reynolds numbers between 2.48×10^5 and 3.91×10^6 at freestream Mach numbers ranging from subsonic to transonic. The formation of the leading-edge laminar separation bubble and the flow separation characteristics at the trailing edge were studied, including the effects of Reynolds number and compressibility. Elliptic airfoils with different thicknesses were considered for the investigation of the thickness effect. The results were compared with those of NACA series airfoils with identical thicknesses.

Nomenclature

a	=	speed of sound
C_d	=	drag coefficient
C_l	=	lift coefficient
C_l/C_d	=	lift-to-drag ratio
C_m	=	moment coefficient about the quarter-chord point
C_p	=	pressure coefficient
c	=	airfoil chord length
f^*	=	nondimensional frequency of aerodynamic force oscillation, $c/2\pi a$
M_∞	=	freestream Mach number
Re	=	Reynolds number based on the airfoil chord length
S	=	control surface
St	=	Strouhal number based on the airfoil chord length, $(f^*c)/M_\infty$
T^*	=	nondimensional period of aerodynamic force oscillation, $1/f^*$
U	=	freestream velocity
V	=	control volume
x	=	distance from the airfoil leading edge
α	=	angle of attack, deg

I. Introduction

THE flow around an elliptic cylinder or an elliptic airfoil has been frequently investigated not only for understanding the fundamental physics of flow, such as unsteady flow separation or self-induced oscillation, but also for practical engineering application purposes. Elliptic airfoils exhibit aerodynamic characteristics different from those of conventional airfoils, due to their unique geometric configuration. At the same maximum thickness, elliptic airfoils have a smaller leading-edge radius than conventional airfoils with a sharp trailing edge. Also, the maximum thickness of an elliptic airfoil is located in the middle of the chord.

Until recently, several studies have been conducted for the investigation of the flow around an elliptic cylinder or an elliptic airfoil based on theoretical, experimental, and numerical methods. Takallu and Williams III [1] theoretically investigated the flow around a 6:1 elliptic cylinder by obtaining steady-state lift coefficients at various angles of attack and unsteady lift hysteresis when the cylinder oscillated in pitch. In their analysis, it was assumed that when the flow separates, the steady-state pressure coefficient of the upper surface decays exponentially from the value at the separation point to zero in the far wake, whereas that of the lower surface varies linearly from the separation point to the trailing edge. Modi and Wiland [2] conducted an experimental study about stationary elliptic cylinders with the eccentricities of 0.6 and 0.8 at subcritical Reynolds numbers between 3×10^3 and 1×10^5. They measured unsteady pressure, lift coefficient, and wake geometry as a function of angle of attack. Kim [3] carried out a numerical study about elliptic cylinders with the eccentricities of 0.6, 0.8, 1.0, and 1.2 at Reynolds numbers of 200, 400, and 1000 and presented the variation of the aerodynamic forces in time for different Reynolds numbers and thicknesses. Lugt and Haussling [4] numerically investigated the evolution of unsteady separated flow around an elliptic cylinder after an impulsive start from rest at an angle of attack of 45 deg for low Reynolds numbers of 15, 30, and 200. Blodgett et al. [5] studied unsteady separated flow around an elliptic cylinder after the flow settled down into a limited-cycle oscillation at 0- and 15-deg angles of attack and a Reynolds number of 1000.

Even though these previous studies provided some insights into understanding the aerodynamic characteristics of elliptic airfoils, most of them were focused mainly on the development of the trailing-edge vortices alternately shedding from relatively thick elliptic cylinders or the behavior of unsteady aerodynamic forces at quite low Reynolds numbers below 1000. Therefore, the aerodynamic characteristics of elliptic airfoils at high Reynolds numbers in the range of practical engineering applications are rarely known.

Hoerner and Borst [6] conducted an experimental study about an elliptic airfoil at high Reynolds numbers of 2×10^6 and 7×10^6. However, the results were limited to the steady lift variation as a function of angle of attack. Kwon [7] experimentally studied the effect of flow transition on the aerodynamic forces of three elliptic airfoils with different thicknesses for Reynolds numbers between 3×10^5 and 8×10^5. The results showed that a considerable difference in the aerodynamic characteristics exists between natural transition and forced transition, mainly due to the different behaviors of the trailing-edge vortices.

In the present study, the aerodynamic characteristics of elliptic airfoils were numerically investigated at relatively high Reynolds numbers between 2.48×10^5 and 3.91×10^6. The flow separation characteristics such as the leading-edge laminar separation bubble and the trailing-edge flow separation were studied, including the effects of Reynolds number and compressibility. The effect of airfoil

Received 7 June 2007; accepted for publication 25 September 2007.

*Ph.D. Candidate, Department of Aerospace Engineering, 373-1 Guseong-dong, Yuseong-gu.

†Professor, Department of Aerospace Engineering, 373-1 Guseong-dong, Yuseong-gu; ojkwon@kaist.ac.kr. Senior Member AIAA (Corresponding Author).

thickness on the aerodynamic characteristics of elliptic airfoils was also investigated. The results were compared with those of conventional airfoils with identical maximum thicknesses at the same flow conditions.

II. Numerical Method

A. Governing Equations

The two-dimensional, time-dependent, Reynolds-averaged Navier–Stokes equations for an ideal gas may be written in an integral form for an arbitrary control volume Ω with the boundary $\partial\Omega$:

$$\frac{\partial}{\partial t}\int_{\Omega} Q\,\mathrm{d}V + \int_{\partial\Omega} F(Q)\cdot \boldsymbol{n}\,\mathrm{d}S = \int_{\partial\Omega} G(Q)\cdot \boldsymbol{n}\,\mathrm{d}S \qquad (1)$$

where Q is the vector of the conservative flow variables; $F(Q)$ and $G(Q)$ are the inviscid and viscous flux vectors in the standard conservation form, respectively; and $\boldsymbol{n}$ is the unit normal vector out from the control volume boundary. The flow variables were nondimensionalized by the freestream quantities, and the length was normalized by the airfoil chord length.

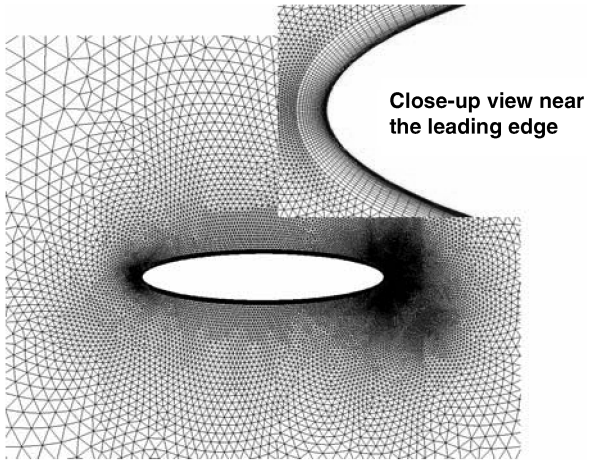

Fig. 1 Hybrid mesh around a 20%-thick elliptic airfoil.

B. Discretization

A vertex-centered finite volume method was employed for the spatial discretization of the governing equations. The computational domain was divided into a finite number of control volumes which were constructed by connecting the median duals surrounding each vertex of unstructured mesh elements. The discretized form of Eq. (1) for each control volume surrounding vertex i and its dual face j can be written as

$$V_i\frac{\partial Q_i}{\partial t} + \sum_{j=1}^{N\text{face}}(F_{ij} - G_{ij})S_{ij} = 0 \qquad (2)$$

where Nface represents the total number of dual faces for the ith control volume. The inviscid flux across each dual face j was computed using Roe's flux-difference splitting formula [8]. A linear reconstruction method based on the least-squares procedure was implemented to achieve second-order accuracy in space. For the evaluation of the viscous flux terms at the dual faces, the thin shear-layer approximation [9] was employed to ensure positive discretization and grid transparency.

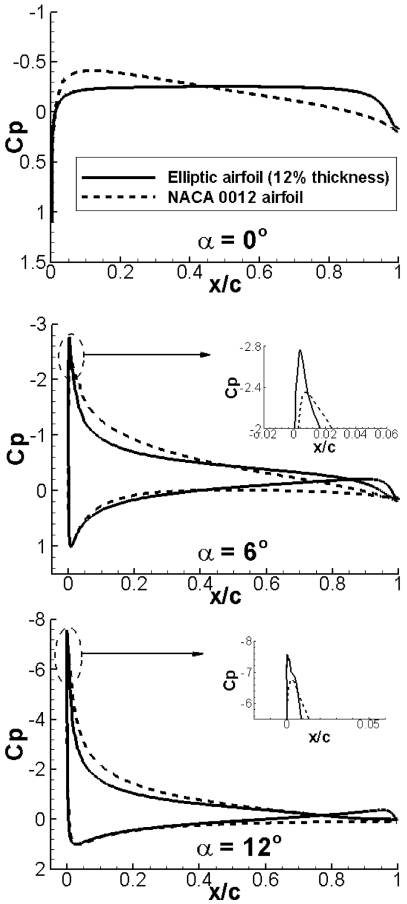

a) Surface pressure distributions

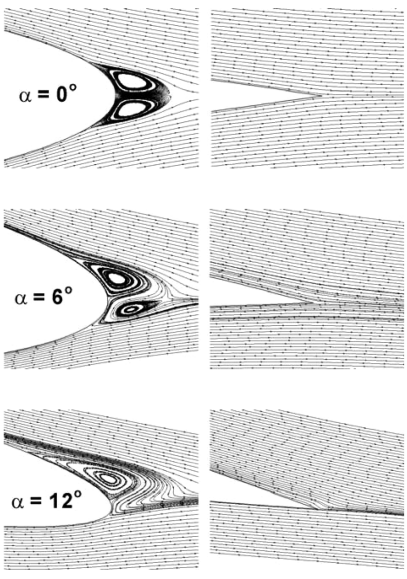

b) Streamline patterns at the trailing edge

Fig. 2 Comparison of surface pressure distributions and corresponding streamline patterns at the trailing edge between a 12%-thick elliptic airfoil and a NACA 0012 airfoil at $M_\infty = 0.3$ and $Re = 3.91 \times 10^6$.

The discretized form of Eq. (2) can be rewritten as a set of differential equations:

$$V_i \frac{\partial Q_i}{\partial t} + R(Q_i) = 0 \qquad i = 1, 2, 3, \ldots \tag{3}$$

where $R(Q_i)$ is the residual of the inviscid and viscous fluxes.

An implicit time-integration algorithm based on the linearized Euler backward differencing was used to advance the solution in time. For unsteady calculations, a dual-time-stepping procedure was employed to allow a relatively large time step size, as well as to reduce the error associated with the linearization procedure. The resultant linear system of equations at each time step was solved using a point Gauss–Seidel method.

C. Computational Details

A characteristic boundary condition was imposed at the far-field boundary, and the no-slip isothermal boundary condition was applied at the solid surface.

For turbulence closure, the Spalart–Allmaras one-equation turbulence model [10] was employed. The source terms and the convection terms of the equation were implemented as suggested by Ashford [11]. Discretization of the diffusion terms and time

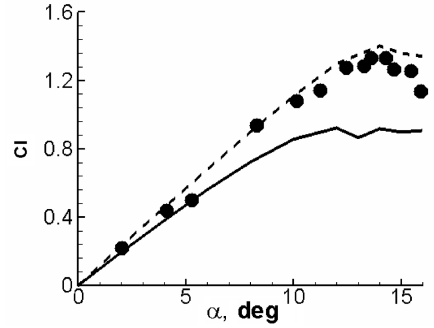

a) Lift coefficient

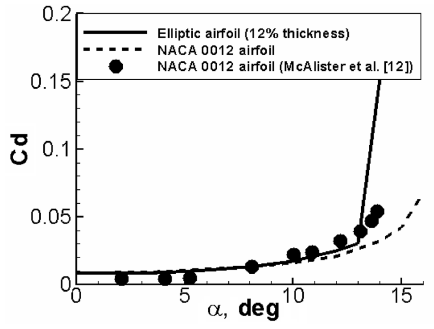

b) Drag coefficient

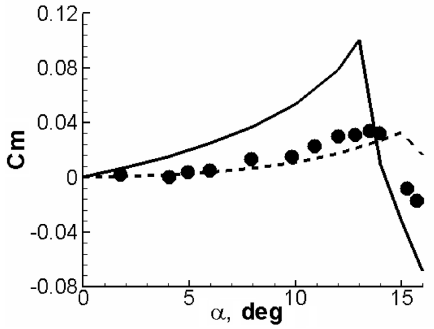

c) Moment coefficient

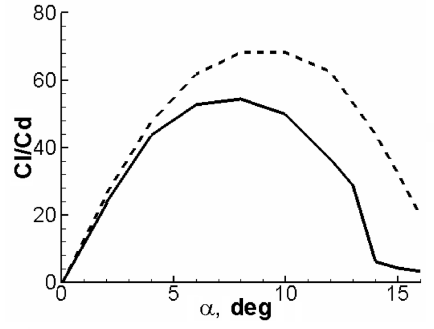

d) Lift-to-drag ratio

Fig. 3 Comparison of aerodynamic force and moment coefficients between a 12%-thick elliptic airfoil and a NACA 0012 airfoil at $M_\infty = 0.3$ and $Re = 3.91 \times 10^6$.

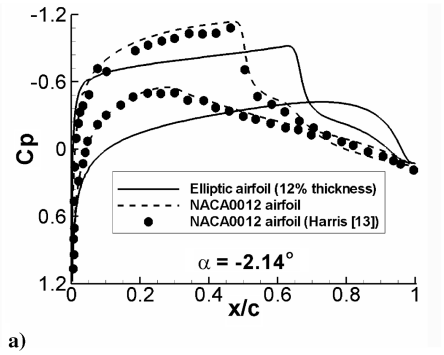

a)

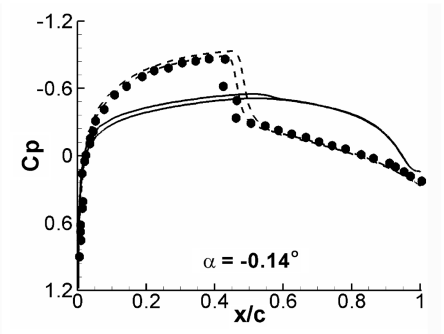

b)

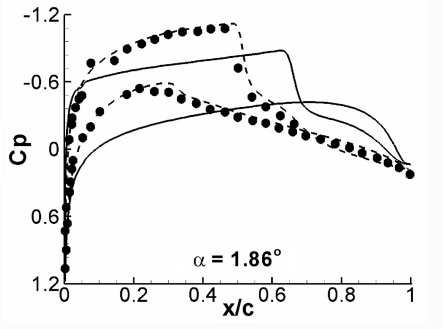

c)

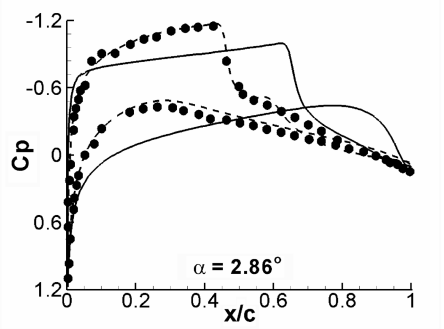

d)

Fig. 4 Comparison of surface pressure distributions between a 12%-thick elliptic airfoil and a NACA 0012 airfoil at $M_\infty = 0.8$ and $Re = 3.0 \times 10^6$.

integration were made similar to those of the mean flow equations. In the present study, all calculations were performed by assuming that the flow was fully turbulent.

To simulate the viscous shear layer accurately and to avoid the numerical difficulties involved in using highly stretched triangular cells, hybrid unstructured meshes were adopted in the present study. The hybrid meshes consisted of quadrilateral cells inside the boundary layer and in the near-wake region and isotropic triangular cells for the rest of the computational domain, as shown in Fig. 1.

Because the flowfield around an elliptic airfoil is inherently unsteady due to the presence of a pair of vortices at the blunt trailing edge, all calculations were performed in a time-accurate manner. When necessary, the steady-state results were obtained by averaging the periodic time-varying solution.

III. Results and Discussion

A. Comparison of Aerodynamic Characteristics with an Ordinary Airfoil

Initially, the aerodynamic forces and moment of a 12%-thick elliptic airfoil were compared with those of a NACA 0012 airfoil at the same flow condition. Calculations were made for subsonic flows at a freestream Mach number of 0.3 and a Reynolds number of 3.91×10^6. In Fig. 2, the surface pressure distributions of the elliptic airfoil at 0-, 6-, and 12-deg angles of attack and the corresponding streamline patterns at the trailing edge are compared with those of a NACA 0012 airfoil. It shows that at a 0-deg angle of attack, the surface pressure on the elliptic airfoil is nearly constant over most of the airfoil, whereas that of the NACA 0012 airfoil gradually increases after the suction peak. For the angles of attack above 0 deg, the elliptic airfoil showed slightly higher suction peaks, but much quicker pressure recovery on the upper surface than the NACA 0012 airfoil, resulting in less pressure loading. In the case of the elliptic airfoil, the flow separated from both upper and lower surfaces at the trailing edge. As the angle of attack increased above 0 deg, the flow became asymmetric, and the pressure inside the separated flow region that further extended upstream on the upper surface became higher than that of the lower surface, where the flow remained attached to the trailing edge. This caused a reversed-pressure region at the trailing edge for angles of attack above 0 deg.

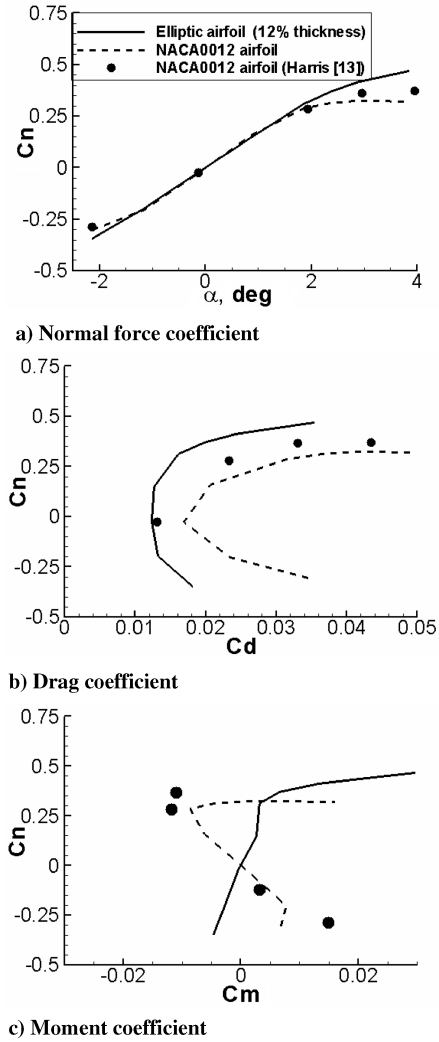

Fig. 5 Comparison of normal force, drag, and moment coefficients between a 12%-thick elliptic airfoil and a NACA 0012 airfoil at $M_\infty = 0.8$ and $Re = 3.0 \times 10^6$.

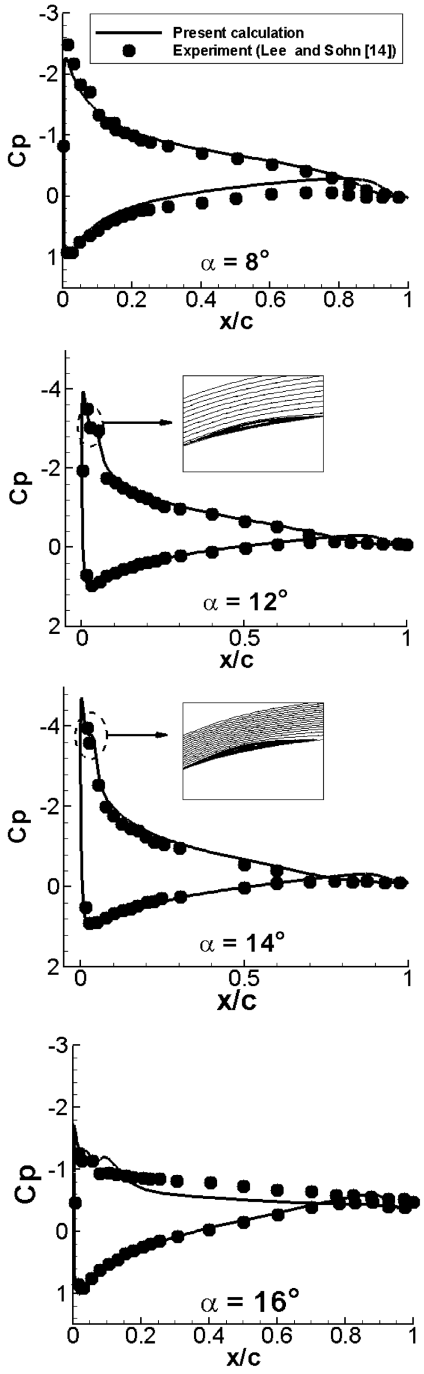

Fig. 6 Comparison of surface pressure distributions between the present calculation and experiment for a 20%-thick elliptic airfoil at $M_\infty = 0.1$ and $Re = 2.48 \times 10^5$.

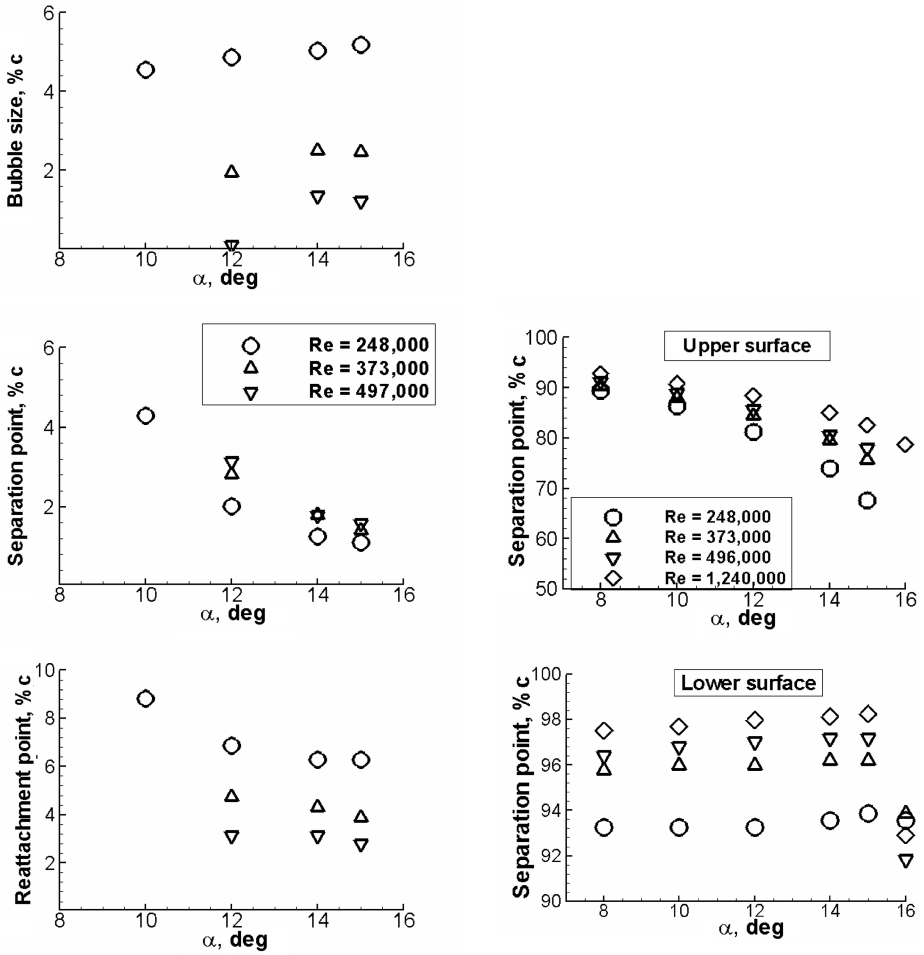

a) Laminar separation bubble b) Trailing-edge separation point

Fig. 7 Effect of Reynolds number on flow separation characteristics for a 20%-thick elliptic airfoil at $M_\infty = 0.1$.

In Fig. 3, the aerodynamic force and moment coefficients are compared between the 12%-thick elliptic airfoil and the NACA 0012 airfoil. It shows that all predicted aerodynamic quantities of the NACA 0012 airfoil are in favorable agreement with the experiment [12]. It was observed that the elliptic airfoil has lower lift and comparable drag compared with the NACA 0012 airfoil below the stall angle of attack. The elliptic airfoil experienced an abrupt drag increase at a lower angle of attack than the NACA 0012 airfoil, due to early stall. As a result, the elliptic airfoil showed an inferior lift-to-drag ratio distribution for all angles of attack considered. As the angle of attack increased, the moment coefficient of the elliptic airfoil continuously increased up to stall, whereas that of the NACA 0012 airfoil remained relatively flat. In summary, the elliptic airfoil showed a poorer aerodynamic efficiency and inferior longitudinal stability characteristics compared with the NACA 0012 airfoil in the present subsonic flow.

To investigate the aerodynamic characteristics of elliptic airfoils in a transonic flow regime, calculations were made for flows around a 12%-thick elliptic airfoil and a NACA 0012 airfoil at a freestream Mach number of 0.8 and at a Reynolds number of 3.0×10^6. In Fig. 4, the surface pressure distributions of the elliptic airfoil at −2.14-, −0.14-, 1.86,- and 2.86-deg angles of attack are compared with those of the NACA 0012 airfoil at the same angles of attack. For the NACA 0012 airfoil, the results predicted by the present calculations are in good agreement with the experimental results [13] for both the shock-wave position and its strength at all angles of attack considered. The shock-induced flow separation and the reversed-pressure region near the trailing edge at high angles of attack were also reasonably well-predicted. At the angle of attack near 0 deg, a shock wave appeared in the middle of the chord for the NACA 0012 airfoil, whereas a shock-free flow was obtained for the elliptic airfoil. As the angle of attack increased, a weaker shock wave appeared on the suction side further downstream. This is because the elliptic airfoil has a smaller leading-edge radius and thus the flow does not accelerate much around the leading edge, compared with the NACA 0012 airfoil. Along the pressure side of the elliptic airfoil, the flow continuously accelerated and the surface pressure gradually decreased, up to approximately 80% of the chord. A slightly larger reversed-pressure region was observed in this transonic flow, compared with the subsonic flow case.

In Fig. 5, the predicted normal force, drag, and moment coefficients of the elliptic airfoil in the transonic flow regime are compared with those of the NACA 0012 airfoil. It shows that for the NACA 0012 airfoil, the predicted lift coefficient was in favorable agreement with the experimental results [13], but the magnitudes of the drag and moment coefficients were slightly off the experimental results, mostly due to the overpredicted reversed-pressure region behind the shock wave, as shown in Fig. 4. Unlike the subsonic flow case, the normal force coefficient at a given angle of attack and its slope of the elliptic airfoil were similar to those of the NACA 0012 airfoil, because comparable loading was obtained ahead of the delayed shock wave. However, at the given normal force, the predicted drag of the elliptic airfoil was slightly lower than that of the NACA 0012 airfoil. Slight nose-up moments were observed for the elliptic airfoil at moderate angles of attack, whereas nose-down moments were observed for the NACA 0012 airfoil. Unlike the previous subsonic flow case, the elliptic airfoil showed a slightly higher aerodynamic efficiency but inferior longitudinal stability characteristics than those of the ordinary airfoil at this transonic flow condition.

B. Flow Separation Characteristics

The flow separation characteristics of elliptic airfoils, such as the leading-edge laminar separation bubble and the trailing-edge flow separation, were investigated in a transition regime. To examine the laminar separation bubble characteristics, the separation and reattachment points and the size of the bubble were assessed. The separation and reattachment points were determined by testing the sign change of the derivative of the streamwise velocity gradient.

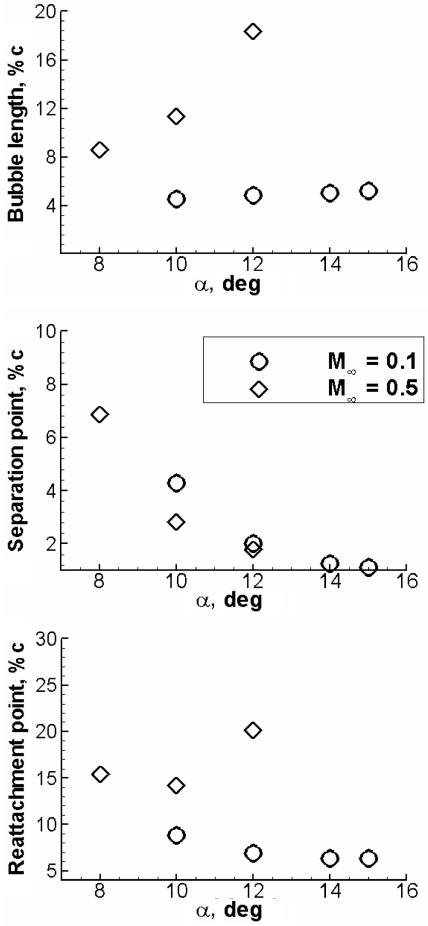

a) Laminar separation bubble

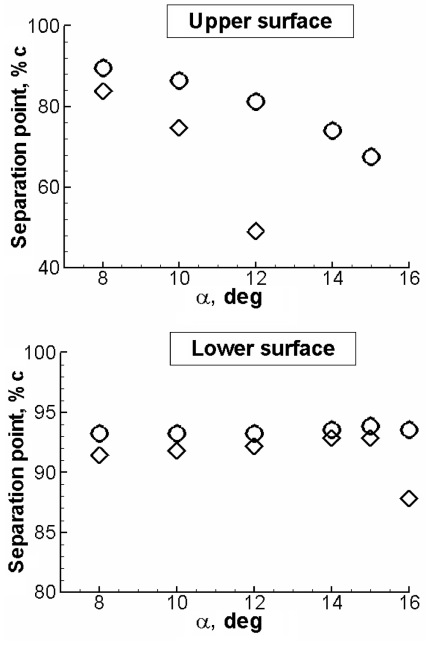

b) Trailing-edge separation

Fig. 8 Effect of compressibility on flow separation characteristics for a 20%-thick elliptic airfoil at $Re = 2.48 \times 10^5$.

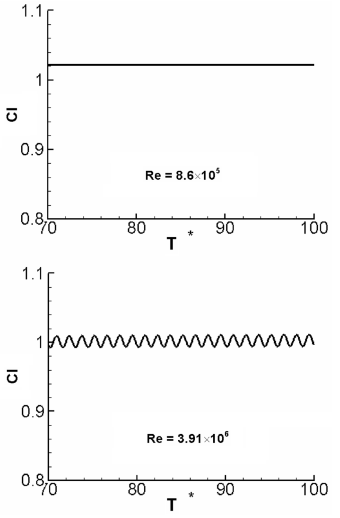

a) 20% thick elliptic airfoil

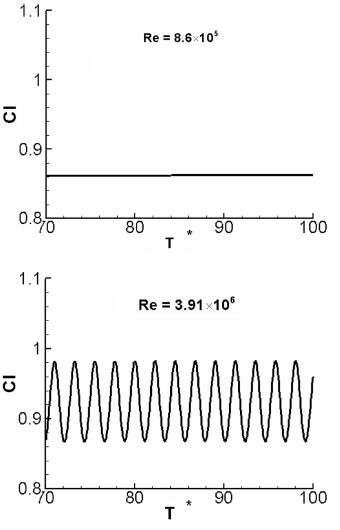

b) 30% thick elliptic airfoil

Fig. 9 Comparison of lift coefficients for 20 and 30%-thick elliptic airfoils between low- and high-Reynolds-number flows at $M_\infty = 0.3$ and $\alpha = 14$ deg.

To validate the capability of the present method of capturing the separation bubble characteristics, calculations were made for flows around a 20%-thick elliptic airfoil at a freestream Mach number of 0.1 and at a Reynolds number of 2.48×10^5. The predicted surface pressure distributions at 8-, 12-, 14-, and 16-deg angles of attack were compared with those of the experiment [14] in Fig. 6. It shows that the predicted results are in good agreement with the experimental data for all angles of attack considered. The constant pressure plateau, which indicated the presence of a laminar separation bubble,

Table 1 Nondimensional frequency and Strouhal number variation at $M_\infty = 0.3$ and $Re = 3.91 \times 10^6$

	20%-thickness airfoil		30%-thickness airfoil	
α, deg	f^*	St	f^*	St
10	·	·	0.50	1.67
12	·	·	0.45	1.52
14	0.71	2.38	0.44	1.47
16	0.63	2.08	0.42	1.39

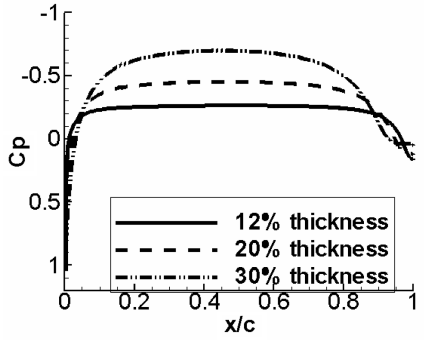

a) $\alpha = 0$ deg

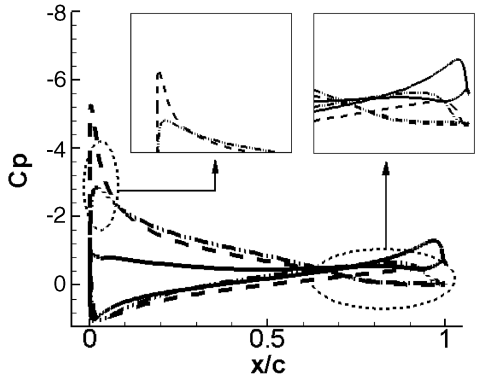

b) $\alpha = 14$ deg

Fig. 10 Effect of thickness on surface pressure distribution at $M_\infty = 0.3$ and $Re = 8.6 \times 10^5$.

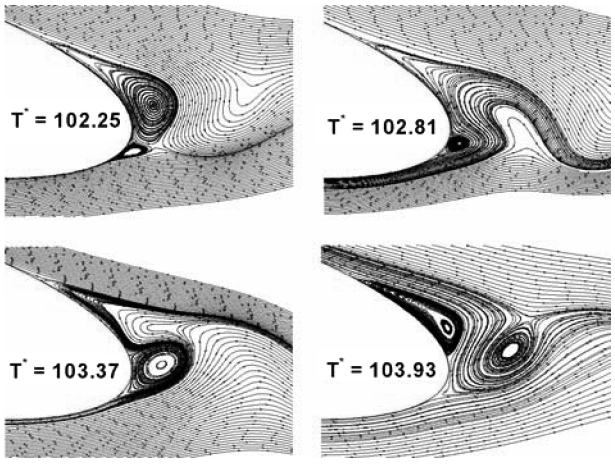

a) Variation of traililng-edge vortices

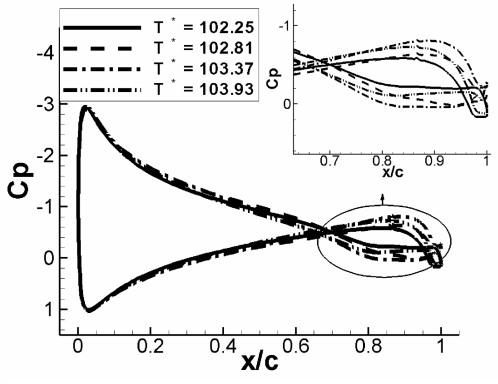

b) Variation of surface pressure distribution

Fig. 11 Variation of trailing-edge vortices in time and related surface pressure distributions for a 30%-thick elliptic airfoil at $M_\infty = 0.3$, $Re = 3.91 \times 10^6$, and $\alpha = 14$ deg.

was also well-predicted at 12- and 14-deg angles of attack. The existence of the laminar separation bubble can also be confirmed by the streamline patterns at the airfoil leading edge. A fully separated flow was observed at a 16-deg angle of attack.

In Fig. 7, the effect of the Reynolds number on the leading-edge laminar separation bubble and the trailing-edge flow separation characteristics was examined by comparing the results for four

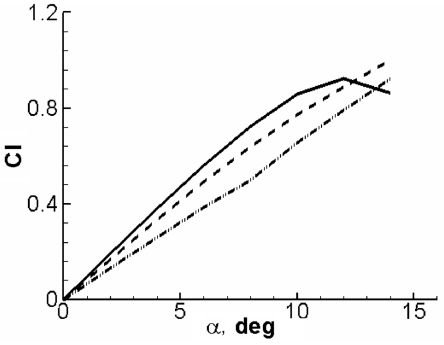

a) Lift coefficient

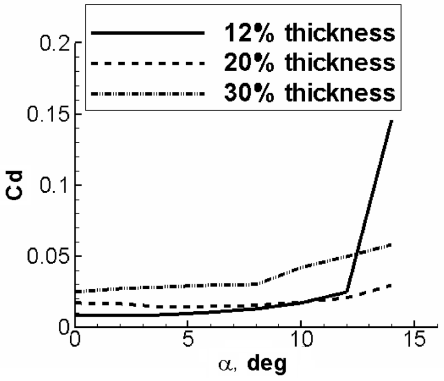

b) Drag coefficient

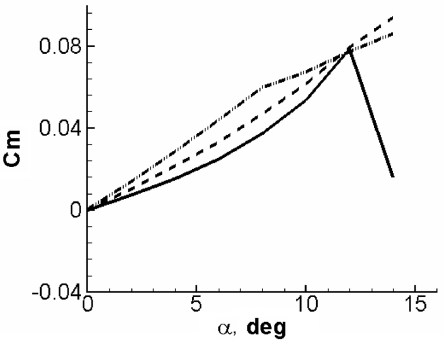

c) Moment coefficient

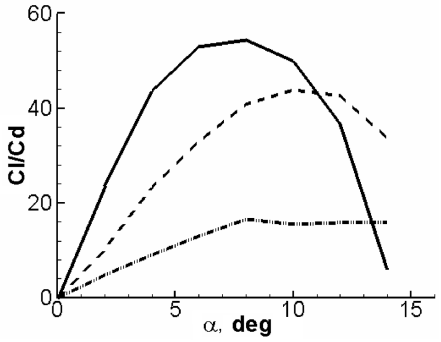

d) Lift-to-drag ratio

Fig. 12 Effect of thickness on aerodynamic force and moment coefficients at $M_\infty = 0.3$ and $Re = 3.91 \times 10^6$.

Reynolds numbers: 2.48×10^5, 3.72×10^5, 4.96×10^5, and 1.24×10^6. Calculations were made for a 20%-thick elliptic airfoil at a freestream Mach number of 0.1. In Fig. 7a, the separation point, the reattachment point, and the laminar separation bubble size are depicted as functions of the angle of attack. The results for the Reynolds number of 1.24×10^6 are not shown in the figure, because laminar separation bubbles were not observed at this Reynolds number for all angles of attack considered. Similar to the ordinary airfoil results [15–17], when the angle of attack increased at a fixed Reynolds number, the separation and reattachment points moved upstream toward the leading edge, and the overall bubble size slightly increased. When the Reynolds number increased at a fixed angle of attack, the reattachment point moved upstream, whereas the separation point location did not change much. As a result, the separation bubble size was reduced as the Reynolds number increased. A similar behavior was also observed for ordinary airfoils [15–17]. In Fig. 7b, the effects of angle of attack and Reynolds number on the location of the trailing-edge separation points are presented. The results show that the upper-surface separation point moved further upstream as the angle of attack increased at a fixed Reynolds number, whereas on the lower surface, the location of the separation point did not change much below stall. The movement of the lower-surface separation point after stall was less than 5% of the chord length. When the Reynolds number increased at a fixed angle of attack, the separation points on both surfaces moved further downstream, mainly due to the delay of flow separation.

In Fig. 8, the effect of compressibility on the laminar separation bubble and the trailing-edge separation points is presented for a 20%-thick elliptic airfoil. The results are compared between freestream Mach numbers of 0.1 and 0.5 at a fixed Reynolds number of 2.48×10^5. At the higher Mach number, the separation point of the bubble was set further upstream for a given angle of attack, whereas the reattachment point was located further downstream. As a result, the size of the laminar separation bubble increased. Also, at the higher Mach number, the upper-surface separation point at the trailing edge was observed further upstream than at the lower-Mach-number flow case, particularly at high angles of attack, causing early stall. However, on the lower surface, the effect of compressibility on

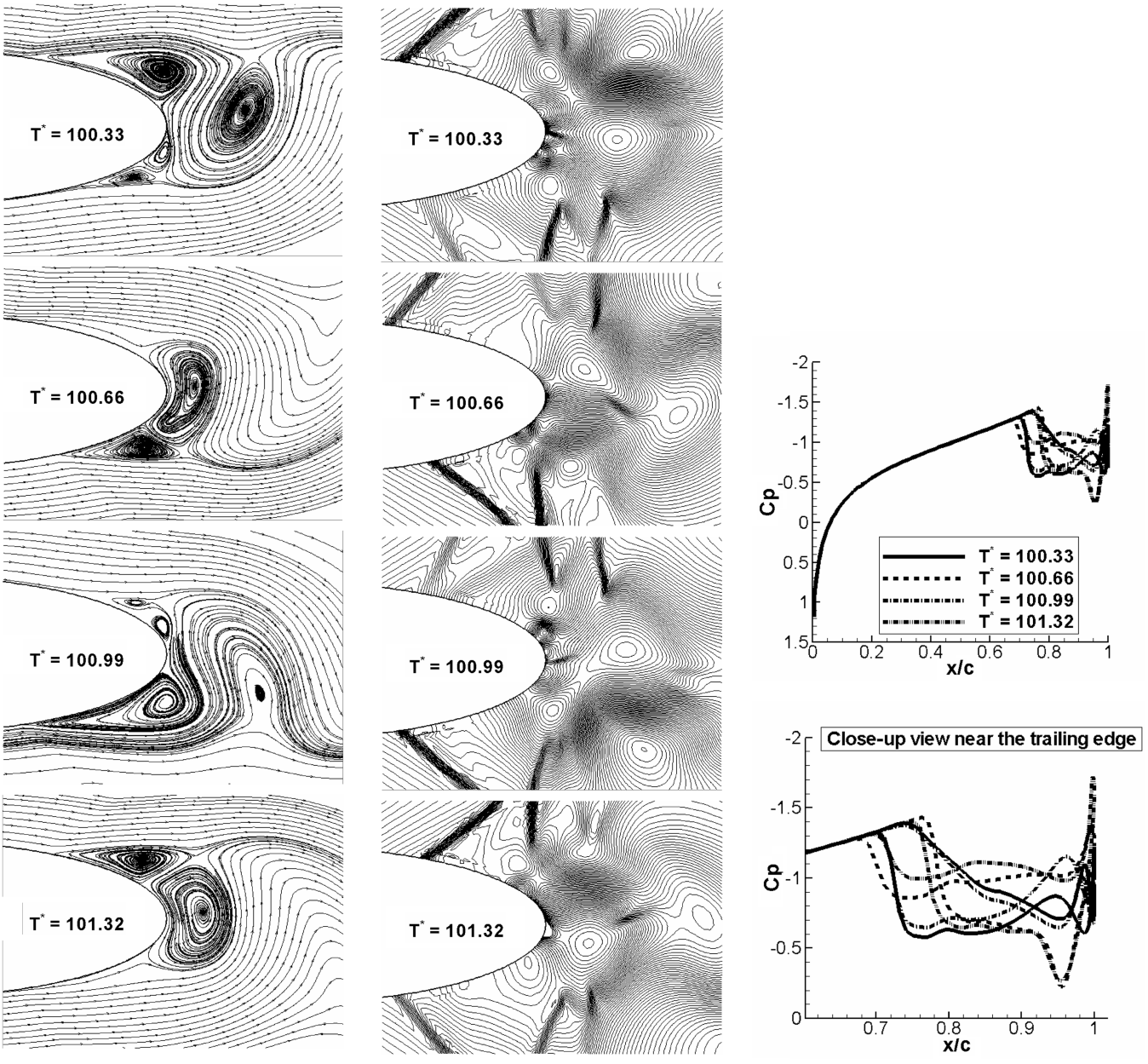

a) Variation of streamlines in time

b) Variation of pressure contours in time

c) Variation of surface pressure distributions in time

Fig. 13 Time-varying flow characteristics of a 30%-thick elliptic airfoil at $M_\infty = 0.8$, $Re = 3.91 \times 10^6$, and $\alpha = 0$ deg.

the separation point was not significant, at least for the angles of attack below stall.

C. Effect of Airfoil Thickness

To examine the effect of airfoil thickness on the aerodynamic characteristics of elliptic airfoils, calculations were made for flows around 12, 20, and 30%-thick elliptic airfoils. In Fig. 9, the unsteady variations of the lift coefficient in time are presented for 20 and 30%-thick elliptic airfoils at a freestream Mach number of 0.3 and a 14-deg angle of attack. It shows that at the lower Reynolds number of 8.6×10^5, the lift coefficients of both 20 and 30%-thick elliptic airfoils were maintained at constant values of 0.858 and 1.004, respectively. However, at the higher Reynolds number of 3.91×10^6, time-varying oscillations of the lift coefficient, caused by the periodic shedding of the trailing-edge vortices, were observed. The amplitude of the oscillation grew larger as the airfoil thickness increased. In Table 1, the nondimensional frequency of the lift variation for the 20 and 30%-thick elliptic airfoils and the corresponding Strouhal number are presented at the Reynolds number of 3.91×10^6. It shows that as the angle of attack increased, both the frequency and the Strouhal number were reduced. A similar trend was also observed when the airfoil thickness increased. The oscillation of lift was not observed for the 12%-thick airfoil at both Reynolds numbers.

In Fig. 10, the surface pressure distributions are compared among 12, 20, and 30%-thick elliptic airfoils at a freestream Mach number of 0.3 and at a Reynolds number of 8.6×10^5. It shows that at a 0-deg angle of attack, the extents of flow acceleration at the leading edge and the deceleration at the trailing edge became larger as the airfoil thickness increased. Also, the pressure on the airfoil surface became lower as the thickness increased. At a 14-deg angle of attack, the magnitude of the suction peak and the chordwise pressure loading decreased as the airfoil thickness increased. Also, the reversed-pressure region at the trailing edge grew larger as the airfoil thickness increased, due to the extended separated flow region on the upper surface. In the case of a 12%-thick airfoil, a fully separated flow was observed on the upper surface at the 14-deg angle of attack, because of the relatively sharp leading edge with a smaller radius of curvature.

In Fig. 11, the instantaneous trailing-edge vortices and the corresponding surface pressure distributions of the 30%-thick elliptic airfoil are presented for the Reynolds number of 3.91×10^6 at a 14-deg angle of attack. It shows that the trailing-edge vortices alternately shed downstream, similar to the turbulent vortex street. The surface pressure was continuously affected by these shedding vortices, especially in the reversed-pressure region at the trailing edge, resulting in the periodic variation of the aerodynamic loads, as shown in Fig. 9.

In Fig. 12, the effect of airfoil thickness on the aerodynamic force and moment coefficients is presented as a function of the angle of attack. The results were obtained at a Reynolds number of 3.91×10^6 by time-averaging each quantity at a given angle of attack. As the airfoil thickness increased, the lift coefficient and its slope were reduced slightly, whereas the drag increased. Also, the stall was delayed up to a higher angle of attack. As a result, the lift-to-drag ratio of the elliptic airfoil became poorer as the thickness increased, but its maximum value was obtained at a higher angle of attack. The magnitude of the moment coefficient below stall grew slightly larger as the thickness increased.

For the examination of the effect of airfoil thickness in transonic flow, calculations were made at a freestream Mach number of 0.8 and at a Reynolds number of 3.91×10^6. In Fig. 13, the instantaneous streamlines, the corresponding pressure contours near the trailing edge, and the surface pressure distributions at selected time levels are presented for a 30%-thick elliptic airfoil at a 0-deg angle of attack. It shows that the limiting streamlines of the trailing-edge vortices were always in contact with the root of the shock waves on both surfaces, and the positions of the shock waves continuously changed in accordance with the shedding of the vortices. As a result of the periodic oscillation of these shock waves, the surface pressure distribution also changed in time downstream of the shock wave. The effect of the shedding vortices was not detected upstream of the shock waves.

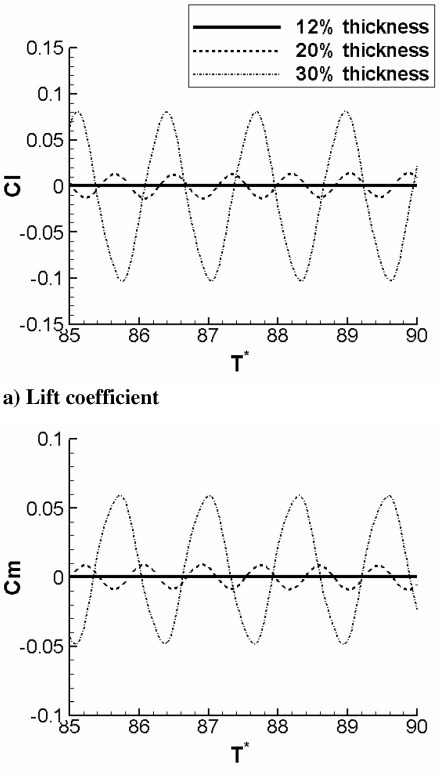

a) Lift coefficient

b) Moment coefficient

Fig. 14 Effect of airfoil thickness on aerodynamic loads of elliptic airfoil at $M_\infty = 0.8$, $Re = 3.91 \times 10^6$, and $\alpha = 0$ deg.

In Fig. 14, the comparison of the aerodynamic loads among the three elliptic airfoils in the transonic flow is presented as a function of time. Periodic oscillations of the aerodynamic loads were observed for airfoils with a thickness of 20% of the chord length or higher, due to the interaction between the shock wave and the shedding vortices, similar to the buffet induced by self-excited shock waves for ordinary airfoils [18,19]. It shows that the periods of oscillation of the lift and moment coefficients are identical, but are in a 180-deg phase difference. The results also show that as the thickness of the airfoil increased, the amplitude as well as the period of oscillation increased for both lift and moment, due to the increment of the shock strength and the trailing-edge vortex strength.

IV. Conclusions

The aerodynamic characteristics of elliptic airfoils were numerically investigated at relatively high Reynolds numbers between 2.48×10^5 and 3.91×10^6 for freestream Mach numbers ranging from subsonic to transonic. It was found that in a fully turbulent subsonic flow, the elliptic airfoil exhibited poorer aerodynamic efficiency and inferior longitudinal stability characteristics, compared with a NACA airfoil with the identical thickness. On the other hand, in a transonic flow, the elliptic airfoil showed slightly better aerodynamic efficiency, but poorer longitudinal stability characteristics. Also, a relatively weaker shock wave was observed further downstream, compared with the NACA airfoil.

In the transition flow regime, leading-edge laminar separation bubbles were observed for moderately thick elliptic airfoils. As the angle of attack increased at a fixed Reynolds number, both separation and reattachment points moved upstream, and the size of the laminar separation bubble slightly increased. When the Reynolds number increased at a fixed angle of attack, the laminar separation bubble size decreased. As the compressibility effect became significant, the bubble size increased proportionally to the angle of attack. At the trailing edge, the flow separated from both upper and lower surfaces

of the elliptic airfoil and a pair of vortices was observed. As the angle of attack increased at a fixed Reynolds number, the flow separation occurred further upstream on the upper surface, whereas on the lower surface, the separation point did not move significantly, even after stall.

When the thickness of the elliptic airfoil increased over 20% of the chord length, periodic variations of aerodynamic loads caused by the shedding of the trailing-edge vortices were observed. As the airfoil thickness increased in subsonic flow, the frequency of oscillation and the Strouhal number decreased, whereas the amplitude of oscillation increased. Also, the time-averaged lift and its slope slightly decreased, whereas drag and the nose-down pitching moment increased. In the transonic flow regime, strong interactions between the shedding vortices and the shock waves were observed, similar to the buffet induced by self-excited shock waves for ordinary airfoils. The amplitude and the period of oscillation increased as the airfoil thickness increased.

Acknowledgment

This study was supported by the research grant from the Underwater Vehicle Research Center of the Agency for Defense Development, Korea. The financial support is gratefully acknowledged.

References

[1] Takallu, M. A., and Williams, J. C., III, "Lift Hysteresis of an Oscillating Slender Ellipse," *AIAA Journal*, Vol. 22, No. 12, 1984, pp. 1733–1741.

[2] Modi, V. J., and Wiland, E., "Unsteady Aerodynamics of Stationary Elliptic Cylinders in Subcritical Flow," *AIAA Journal*, Vol. 8, No. 10, 1970, pp. 1814–1821.

[3] Kim, M. S., "Unsteady Viscous Flow over Elliptic Cylinders at Various Thicknesses with Different Reynolds Numbers," AIAA Paper 2005-5130, June 2005.

[4] Lugt, H. J., and Haussling, H. J., "Laminar Flow Past an Abruptly Accelerated Elliptic Cylinder at 45° Incidence," *Journal of Fluid Mechanics*, Vol. 65, Oct. 1974, pp. 711–734. doi:10.1017/S0022112074001613

[5] Blodgett, K., Ghia, K. N., Osswald, G. A., and Ghia, U., "Unsteady Separated Flow Past an Elliptic Cylinder," *ASME, SIAM, and APS 1st National Fluid Dynamics Congress*, A88-48776AIAA, Washington, DC, 1988, pp. 1383–1390; also .AIAA, Paper 1988-3607.

[6] Hoerner, S. F., and Borst, H. V., "*Fluid-Dynamic Lift: Practical Information on Aerodynamic and Hydrodynamic Lift*," Hoerner Fluid Dynamics, 1975, pp. 2.6–2.7.

[7] Kwon, K. J., "Experimental Study on Aerodynamic and Flow Field Characteristics of Elliptic Airfoils," Ph.D. Dissertation, Dept. of Aerospace Engineering, Korea Advanced Inst. of Science and Technology, Daejeon, Korea, 2006.

[8] Roe, P. L., "Approximate Riemann Solvers, Parameter Vectors, and Difference Scheme," *Journal of Computational Physics*, Vol. 43, No. 2, Oct. 1981, pp. 357–372. doi:10.1016/0021-9991(81)90128-5

[9] Haselbacher, A., McGuirk, J. J., and Page, G. J., "Finite Volume Discretization Aspect for Viscous Flows on Mixed Unstructured Grids," *AIAA Journal*, Vol. 37, No. 2, 1999, pp. 177–184.

[10] Spalart, P. R., and Allmaras, S. R., "A One-Equation Turbulence Model for Aerodynamic Flows," AIAA Paper 92-0439, 1992.

[11] Ashford, G. A., "An Unstructured Grid Generation and Adaptive Solution Technique for High-Reynolds-Number Compressible Flows," Ph. D. Dissertation, Dept. of Aerospace Engineering, Univ. of Michigan, Ann Arbor, MI, 1996.

[12] McAlister, K. W., Pucci, S. L., McCroskey, W. J., and Carr, L. W., "An Experimental Study of Dynamic Stall on Advanced Airfoil Sections," Vol. 2, NASA TM 84245, Sept. 1982.

[13] Harris, C. D., "Two Dimensional Aerodynamic Characteristics of the NACA 0012 Airfoil in the Langley 8-Foot Transonic Pressure Tunnel," NASA TM-81927, 1981.

[14] Lee, K. Y., and Sohn, M. H., "Static Stall Characteristics of Elliptic Airfoil," *Proceedings of the Fall Conference of the Korean Society for Aeronautical and Space Science*, Korean Society for Aeronautical and Space Science, Seoul, Korea, Nov. 2003, pp. 641–646.

[15] Noh, S. K., "Effects of Leading-Edge Separation Bubble on Trailing-Edge Separation for Low Speed Symmetrical Airfoil," M.S. Thesis, Dept. of Aerospace Engineering, Korea Advanced Inst. of Science and Technology, Daejeon, Korea, 1983.

[16] Gault, D. E., "An Experimental Investigation of Regions of Separated Laminar Flow," NACA TN3050, Sept. 1955.

[17] O'Meara, M. M., and Mueller, T. J., "Laminar Separation Bubble Characteristics on an Airfoil at Low Reynolds Numbers," *AIAA Journal*, Vol. 25, No. 8, 1987, pp. 1033–1041.

[18] Levy, L. L., Jr., "Experimental and Computational Steady and Unsteady Transonic Flows About a Thick Airfoil," *AIAA Journal*, Vol. 16, No. 6, 1978, pp. 564–572.

[19] Chung, I. J., "Prediction for Onset of Transonic Shock Buffet Using Steady Thin-Layer Navier–Stokes Solver," Ph.D. Dissertation, Dept. of Aerospace Engineering, Korea Advanced Inst. of Science and Technology, Daejeon, Korea, 2002.